



HAL
open science

Fast X-ray Nanotomography with Sub-10 nm Resolution as a Powerful Imaging Tool for Nanotechnology and Energy Storage Applications

Vincent de Andrade, Viktor Nikitin, Michael Wojcik, Alex Deriy, Sunil Bean, Deming Shu, Tim Mooney, Kevin Peterson, Prabhat Kc, Kenan Li, et al.

► **To cite this version:**

Vincent de Andrade, Viktor Nikitin, Michael Wojcik, Alex Deriy, Sunil Bean, et al.. Fast X-ray Nanotomography with Sub-10 nm Resolution as a Powerful Imaging Tool for Nanotechnology and Energy Storage Applications. *Advanced Materials*, 2021, 33 (21), pp.2008653. 10.1002/adma.202008653 . hal-03545058

HAL Id: hal-03545058

<https://hal.science/hal-03545058v1>

Submitted on 19 Oct 2023

HAL is a multi-disciplinary open access archive for the deposit and dissemination of scientific research documents, whether they are published or not. The documents may come from teaching and research institutions in France or abroad, or from public or private research centers.

L'archive ouverte pluridisciplinaire **HAL**, est destinée au dépôt et à la diffusion de documents scientifiques de niveau recherche, publiés ou non, émanant des établissements d'enseignement et de recherche français ou étrangers, des laboratoires publics ou privés.

Fast X-ray Nanotomography with Sub-10 nm Resolution as a Powerful Imaging Tool for Nanotechnology and Energy Storage Applications

Vincent De Andrade,* Viktor Nikitin, Michael Wojcik, Alex Deriy, Sunil Bean, Deming Shu, Tim Mooney, Kevin Peterson, Prabhat Kc, Kenan Li, Sajid Ali, Kamel Fezzaa, Doga Gürsoy, Cassandra Arico, Saliha Ouendi, David Troadec, Patrice Simon, Francesco De Carlo, and Christophe Lethien

In the last decade, transmission X-ray microscopes (TXMs) have come into operation in most of the synchrotrons worldwide. They have proven to be outstanding tools for non-invasive ex and in situ 3D characterization of materials at the nanoscale across varying range of scientific applications. However, their spatial resolution has not improved in many years, while newly developed functional materials and microdevices with enhanced performances exhibit nanostructures always finer. Here, optomechanical breakthroughs leading to fast 3D tomographic acquisitions (85 min) with sub-10 nm spatial resolution, narrowing the gap between X-ray and electron microscopy, are reported. These new achievements are first validated with 3D characterizations of nanolithography objects corresponding to ultrahigh-aspect-ratio hard X-ray zone plates. Then, this powerful technique is used to investigate the morphology and conformality of nanometer-thick film electrodes synthesized by atomic layer deposition and magnetron sputtering deposition methods on 3D silicon scaffolds for electrochemical energy storage applications.

1. Introduction


Thanks to the short wavelength of hard X-rays and their ability to penetrate matter, transmission X-ray microscopes (TXMs) are well-suited full-field instruments to perform

nano-computed-tomography (nano-CT). They have emerged in many synchrotrons worldwide^[1–6] and have been widely used in energy science where typical spatial resolutions of 30–60 nm and respective field of view (FOV) of about 40–70 μm are ideal for the ex situ or in situ characterization of different type of lithium-ion batteries.^[7–12] However, they can be also utilized to characterize any type of materials like alloys,^[13,14] rocks,^[15] single minerals in solution,^[16,17] polymers,^[18] liquids,^[19] biological tissues,^[20] etc. While 19 nm spatial resolution has been reported in 2D on gold test patterns with long exposure,^[21,22] existing TXMs operating with high brightness synchrotron sources currently provide a maximum resolution of 30 nm.^[23] Projection microscopy, another full-field nano-CT technique, has the

potential of achieving sub-20 nm spatial resolution. However, the best 3D resolution reported so far is 55 nm.^[24] The constant and rapid development of manufactured nanomaterials and the societal and economic stakes associated with them are important drivers for improving the resolving power of X-ray microscopes.

Dr. V. De Andrade,^[†] Dr. V. Nikitin, Dr. M. Wojcik, A. Deriy, S. Bean, Dr. D. Shu, Dr. T. Mooney, K. Peterson, Dr. P. Kc,^[††] Dr. K. Fezzaa, Dr. D. Gürsoy, Dr. F. De Carlo
X-ray Science Division
Advanced Photon Source
Argonne National Laboratory
Argonne, IL, USA
E-mail: vdeandrade@sigray.com

Dr. K. Li, S. Ali
Applied Physics
Northwestern University
Evanston, IL 60208, USA

 The ORCID identification number(s) for the author(s) of this article can be found under <https://doi.org/10.1002/adma.202008653>.

^[†]Present address: Sigray, Inc., 5750 Imhoff Drive, Suite I, Concord, CA 94520 USA

^[††]Present address: DIDS/OSEL/CDRH, The Food and Drug Administration, 25 New Hampshire Avenue, Silver Spring, MD 20903, USA

DOI: 10.1002/adma.202008653

Dr. K. Li
Stanford Synchrotron Radiation Lightsource
SLAC National Accelerator Laboratory
Menlo Park, CA 94025, USA

Dr. C. Arico, Dr. S. Ouendi, Dr. D. Troadec, Dr. C. Lethien
Institut d'Electronique, de Microélectronique et de Nanotechnologie
Université de Lille
CNRS
Centrale Lille Institut
YNCREA-ISEN
Université Polytechnique des Hauts de France UPHF
CNRS UMR 8520-IEMN, Lille F-59000, France

Dr. C. Arico, Dr. P. Simon
Centre Interuniversitaire de Recherche et d'Ingénierie des Matériaux (CIRIMAT)
CNRS UMR 5085 – Université Paul Sabatier
Toulouse 31062, France

Dr. C. Arico, Dr. S. Ouendi, Dr. D. Troadec, Dr. P. Simon, Dr. C. Lethien
Réseau sur le Stockage Electrochimique de l'Energie (RS2E)
CNRS FR 3459, Amiens Cedex 80039, France

A typical example illustrating this trend is Moore's law for semiconductor and microelectronics industry.^[25] This law refers to the fact that the number of transistors on a microchip doubles every 2 years. Intel has recently achieved 14 nm transistor technology with 8 nm large fins. To date, ptychography is the X-ray technique achieving the highest 3D spatial resolution. With hard X-ray, 14.6 nm resolution (with 14.3 nm voxel size) estimated with the Fourier shell correlation (FSC) methods has been reported on integrated circuits^[26] but this scanning technique suffers from long acquisition time since 22 h were necessary to measure a 10 μm large cylindrical sample. With soft X-ray ptychography, 11 nm spatial resolution was reported on a battery material,^[27] but the sample volume was limited to 250 nm, value corresponding to the depth of field (DOF) of the instrument. Therefore, full-field imaging instruments remain an appealing alternative to combine high throughput and high resolution. In this context, we have built an in-house TXM at Sector 32-ID of the advanced photon source at Argonne National Laboratory that is geared toward flexibility and performance in terms of speed and spatial resolution.^[1] This highly modular microscope can accommodate all sorts of sample environment cells as well as different kinds of X-ray optics (Figure S1, Supporting Information). Recently, 16 nm outermost zone width (Δr_N) Fresnel zone plate (FZP) objective lenses have been developed in-house and incorporated into the TXM system to upgrade its scope of capabilities. Those lenses are coupled with a monocapillary condenser fabricated by Sigray Inc. who recently improved its manufacturing process to better control the slope errors of those ellipsoidal optics. For the 8–9 keV energy range, 16 nm Δr_N FZP could potentially lead to a resolving power as low as 9.6 nm with optimum partially coherent illumination.^[28,29] A spatial resolution equivalent to the resolution limit of the objective lens can be achieved only if FZP and sample show relative vibrational stability better than the targeted resolution. For this purpose, an ultrastiff sample stack and FZP module has been built (Figure S1c,e, Supporting Information). To extend this resolution to 3D reconstructions, relative drifts occurring during nano-CT scans as well as the runout of the rotary stage have to be kept below the resolution limit or corrected afterward with software registration. In this contribution, the resolving power of the TXM as well as the ability to maintain spatial resolution on 3D tomographic reconstructions is first established on 2D and 3D test patterns. Then, the potential of high-resolution X-ray nano-CT is demonstrated through two applications. The first one consists in performing without any sectioning in depth fast failure analysis and defect characterization of high-resolution 16 nm Δr_N FZPs optics located on a same silicon chip. The second investigated application relates to electrochemical energy storage miniaturized devices based on T-Nb₂O₅ niobium pentoxide electrode. This study aims at analyzing the conformal deposition of T-Nb₂O₅ films on 3D silicon microtubes scaffold by two different production compatible deposition methods, atomic layer deposition (ALD) and magnetron sputtering (MS).

2. Results and Discussion

2.1. Instrumental Performances

The optical performance of the TXM is first assessed on 2D X-ray absorption images of a Siemens star test pattern as well

as a new type of high-aspect-ratio FZP fabricated with metal-assisted chemical etching (MACE)^[30] with 16 nm thick platinum ALD metalized zones (Figure 1). In addition to being used as nanofocusing optics,^[31] these FZPs can be considered as test objects thanks to their well-controlled wall thickness and known geometry. Both images were acquired at 8 keV. The Siemens star consists in spokes radially converging toward its center. In the central part, separations between the spokes smaller than 20 nm are spatially resolved on the transmission X-ray microscopy and SEM control images (Figure 1b,c). Some of the spokes seem to be fused together. Because such features are visible and correlated on both transmission X-ray microscopy and SEM images, one can conclude that they are real and not resulting from a lack of resolution. On the radiographs of the FZP used as a test object, 16 nm thick Pt walls that were grown by ALD are clearly resolved, as it is illustrated in Figure 1d,e and on the intensity profile Figure 1f. Subtle variations in apparent wall thickness and absorption can be explained by light local warping of walls in the third dimension as shown later in the 3D analysis of this optic. Those direct observations demonstrate that the resolving power of the microscope is at least 16 nm, but to estimate the resolution limit, the Fourier ring correlation (FRC) method^[32] has been applied on pair of radiographs of the FZP acquired with exposure time ranging from 1 to 30 s with 5.2 nm pixel size (see Supporting Information). The FRC with the half-bit criterion indicates a spatial resolution of 9.4 nm. It is consistent with theoretical resolution ranging from 0.6 to 0.8 times the Δr_N of FZP in case of partially coherent illumination.^[21] The dependence of spatial resolution with exposure time is described in Figure 1h. It shows for instance that 1 s exposure only provides 17 nm spatial resolution while 11 s are necessary to achieve 10 nm. The optimum resolution of 9.4 nm is reached after 20 s.

Then, the ability to perform high-resolution 3D imaging is demonstrated through two tomographic datasets of different 1 μm thick MACE FZPs from a same fabrication batch (Figures 2 and 3). 3D reconstructions presented in this contribution have been performed using a distributed optimization framework for tomographic imaging of samples at the nanoscale.^[33] (See Supporting Information). This framework corrects for thermal drifts, the runout of the rotary stage which is of the order of 20 nm, and potential nanoscale sample deformation under the intense synchrotron X-ray beam during the full tomographic acquisitions. The full FZPs, with a diameter of 150 μm are ten times bigger than the 14 \times 16 μm^2 TXM FOV. Neither focused ion beam (FIB) nor laser sectioning were performed to reduce the sample to a size matching the FOV of the TXM. Consequently, local tomographies were performed on intact FZPs with a missing wedge of $\pm 20^\circ$ corresponding to an angular interval where the sample is completely absorbing X-ray. The tomograms correspond to 15 μm large areas located 20 μm away from the FZP edge and in the outermost part of the FZP. They were acquired at 8 keV in interlaced step scan mode with 5.2 nm large voxels (Figures 2 and 3). A 5.2 nm sampling frequency sets the maximum achievable resolution to 10.4 nm (two voxels). To estimate the spatial resolution that can be achieved in 3D with the 32-ID TXM, the FSC method has been applied to one of the tomograms. FSC is a 3D extension of FRC. Because this technique requires to split one dataset in two halves (see Supporting Information), a very large 3D

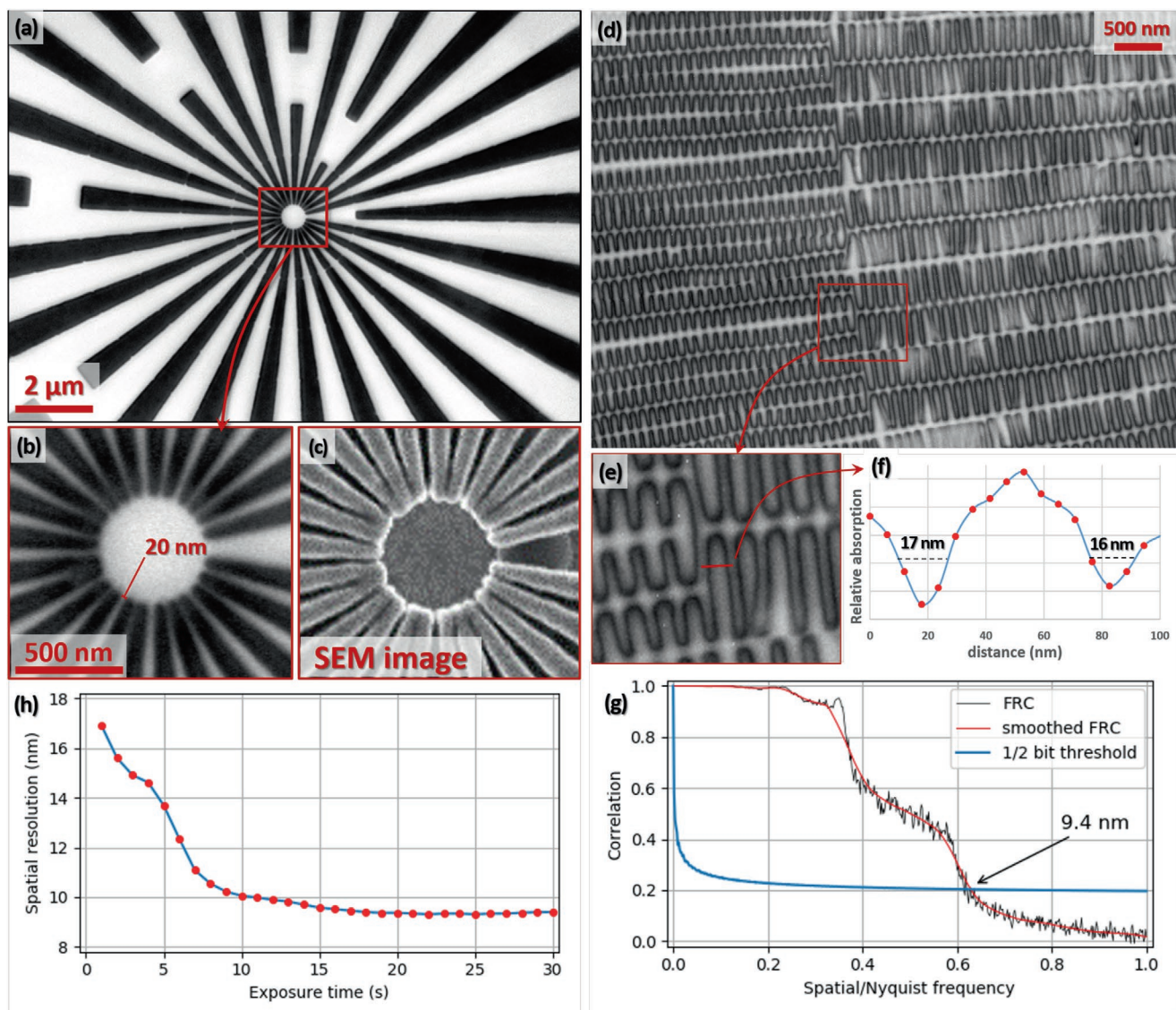


Figure 1. Spatial resolution of the TXM. a) 20 s exposure transmission X-ray microscopy radiograph of a Siemens star test object. b) Zoom on the central part of the Siemens star imaged with the TXM. c) High-resolution SEM image of the region shown in (b) used to validate the transmission X-ray microscopy radiograph. Both images highlight that some tips of the star spokes have fused because of over-plating and that spacing smaller than 20 nm are spatially resolved. d) 30 s exposure radiograph of an area close to the outermost part of a 16 nm Δr_N FZP taken with 30 s exposure. Walls are about 17 nm thick. e) Zoom on a region of the radiograph shown in (d). f) 100 nm long intensity profile corresponding to the red line shown in (e). g) FRC applied on this image return 9.4 nm spatial resolution with the half-bit threshold. h) Spatial resolution expressed as a function of exposure time.

dataset of 5000 projections with 3 s exposure each has been acquired in 250 min while the resolution estimate corresponds to acquisition time of 125 min. Since the sample is very anisotropic ($14 \times 16 \times 1 \mu\text{m}^3$), FSC has not been calculated on a large cubic matrix that would mainly comprise empty voxels. Instead, a local resolution map covering the entire sample was computed applying FSC on 20×33 cubic matrices of the size 256^3 sliding along an XY grid with 64 voxels steps (Figure 2e). This map shows that the resolution level is below 10 nm in the large majority of the reconstructed volume and slightly degrades down to 12 nm on the borders. The FSC plot of one of the central cubes is shown in Figure 2d. Despite two unfavorable measurement conditions corresponding to the missing

wedge and local tomography, the spatial resolution of the 3D dataset is quasi-equivalent to the 2D spatial resolution of the TXM estimated above at 9.4 nm with FRC. These estimates are also supported with direct observations. For instance, the 3D reconstructions enable to clearly resolve 16 nm large walls as shown on volume renderings, reconstructed slices, and line profiles of Figures 2 and 3. The most convincing observations correspond to areas where walls are in very close proximity. Selected slices of Figure 3c,d with their corresponding profiles Figure 3c',d' show that object separations as tiny as 10 nm can be resolved. The drop of contrast observed in the profiles indicates that 10 nm is close to the resolving power limit. One should note that the tomographic reconstruction

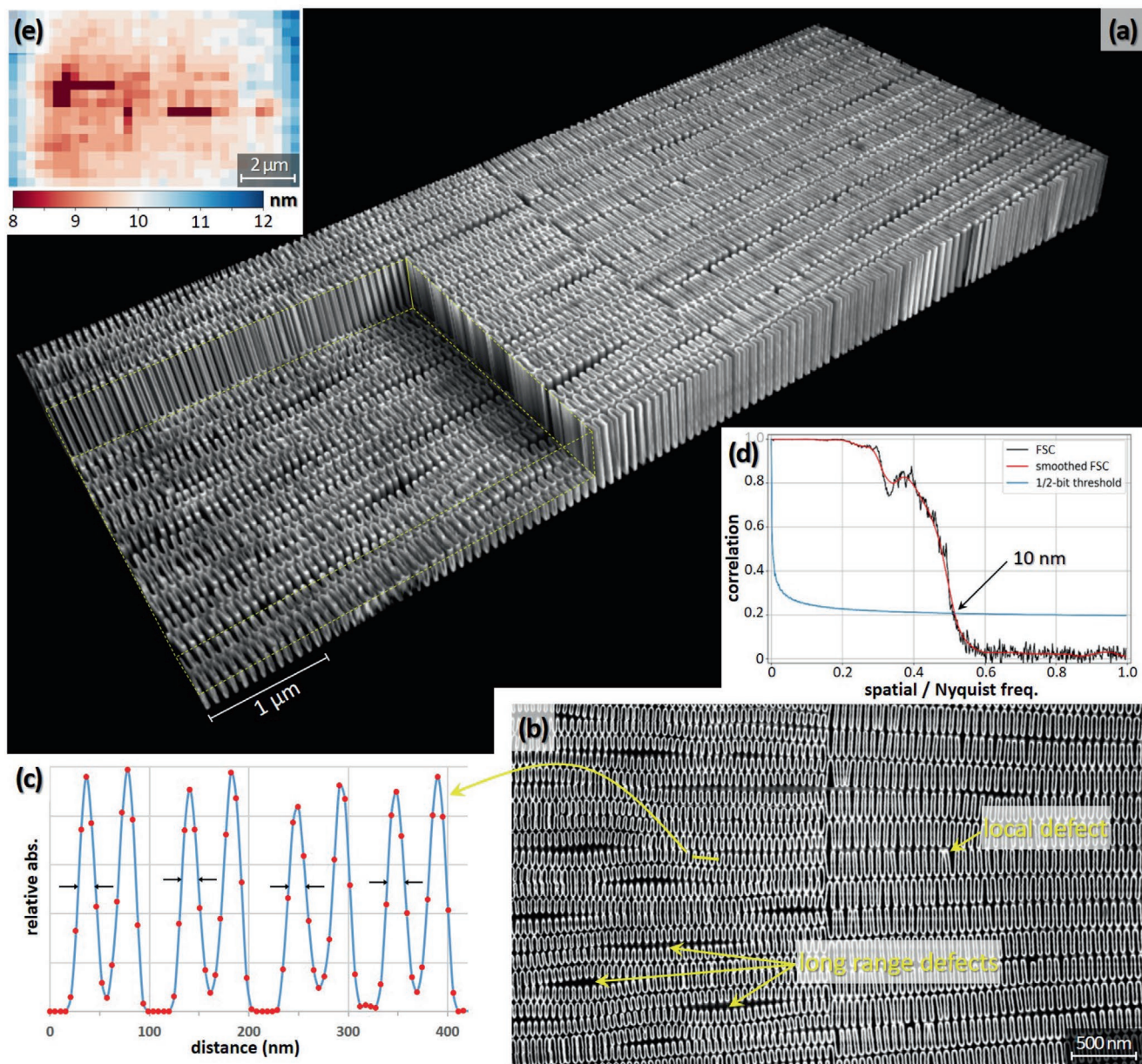


Figure 2. 3D characterization of 16 nm Δr_N FZP. a) Volume rendering with the Dragonfly ORS of a 1 μm thick MACE FZP with 16 nm thick walls coated with Pt. A sub-volume materialized with yellow lines has been removed from 3D visualizations to unravel in-depth structures also visible on the cross sections. b) Zoom on a selected reconstructed slice inside the optic showing 16 nm wide Pt walls deposited by ALD. Local and long range defects are highlighted with yellow arrows. c) Intensity profile showing the periodical arrangement of the walls. The distance between the black arrow tips corresponds to 16 nm. d) FSC applied on a 256^3 voxels large cube returns sub-10 nm spatial resolution with the half-bit threshold. e) Spatial resolution map computed with local FSC calculations performed on 20×33 cubes made of 256^3 voxels each.

algorithm used to compensate for potential sample drifts and deformation has been applied to realign the projections.^[33] While no sample deformation was detected, light sample drift was retrieved and corrected by software translation during reconstruction. The shift average and standard deviation were respectively 5.3 and 3.5 nm. Correcting the drift led to spatial resolution enhancement from 16 to 10 nm. The presented results are compared to the state of the art for three different hard X-ray nano-CT techniques in Table S2, Supporting Information.

2.2. Nanolithography Application

The second part of this work illustrates with two different applications the potential of high-resolution transmission X-ray microscopy nano-tomography for two different applications in materials science. The first application consists in characterizing non-invasively the MACE FZPs shown in the precedent section related to the spatial resolution. Here, nano-CT is used as a diagnostic tool to seek for potential defects that can occur while etching operates below the surface. With MACE,

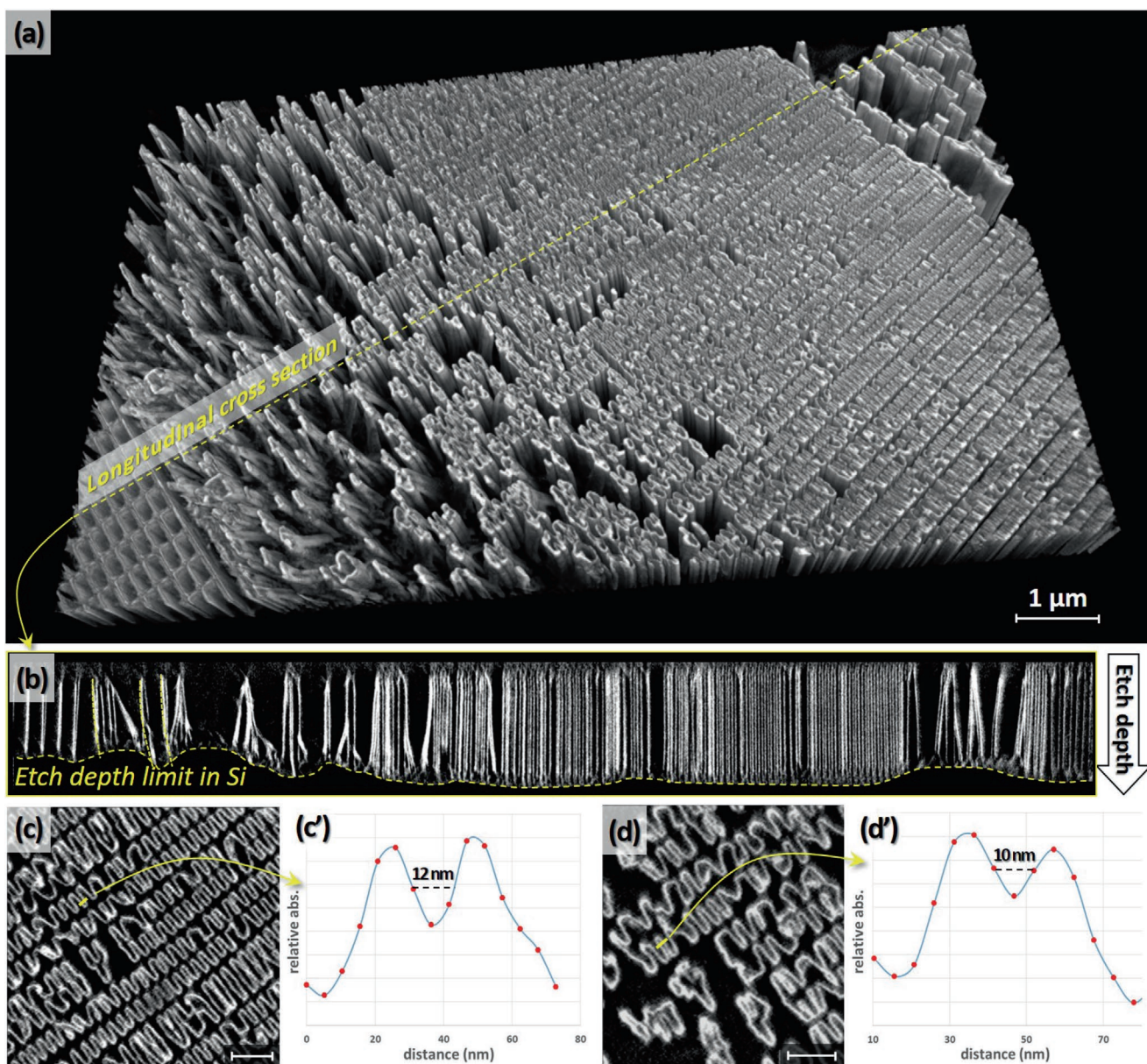


Figure 3. 3D characterization of a defective 16 nm Δr_N FZP. a) Volume rendering with the Dragonfly ORS software of the outermost part of a 1 μm thick FZP where most of damages are seen. b) Longitudinal cross section highlighting large variations in the etch profile, collapsed walls, and large portions of missing zones. c,d) Zoom on selected reconstructed slices showing disorganization of walls geometry. Scale bars correspond to 250 nm. c',d') Short profiles showing that 10 nm spacing between objects can be resolved. Because 10 nm also corresponds to the resolution limit, the contrast between walls and interstice is here significantly lower than in Figure 2c.

several micrometers deep etch was achieved on FZP and ALD, was then used to metalize the MACE-produced silicon FZP by depositing a thin layer of platinum to double the zone frequency. The nano-CT results unravel 3D structures that cannot be seen with SEM images without destroying the FZPs by cross-sectioning or cleaving process. The principal highlight of this high-resolution 3D characterization is the localized defect of the FZP walls generated from meandering etching paths. In MACE, a very thin layer of gold was used as a catalyst to etch into silicon. To fabricate these high-resolution FZP, 15 nm gold layer was used. Such a thin etching catalyst layer lacks

mechanical stability and easily deforms. As can be seen on the 3D rendering of Figure 2a and the reconstructed slice selected under the object surface (Figure 2b), the etching pattern began to deviate from the original FZP pattern as MACE proceeded. Tomography from a defective FZP in Figure 3b shows that close to the FZP perimeter, the etch front depth along the radial direction is uneven (yellow dashed line) and missing zones and collapses are also observed. Unlike what is observed of the FZP 3D rendering of Figure 2a, these defects are sufficiently pronounced to emerge to the surface as underscored by Figure 3a. These defects result from an overexposed e-beam lithography

process and incomplete lift-off process before MACE. Nano-CT can therefore be very useful to identify the best FZP fabricated on the same chip. The vertical profiles extracted from the 3D volume of the MACE FZP also provide evidences such as etch depth and etch front uniformity for us to further improve the fabrication process for better optical performance. Local defects can also be spotted in areas globally undisturbed, as pointed by the yellow arrow in Figure 2b. In sum, this application demonstrates the capability of high-resolution nano-CT with transmission X-ray microscopy to perform non-invasive fast failure analysis/defect characterization of fabricated nanostructures and manufactured nanomaterials. These measured 3D volumes could also serve as input for more accurate focusing optics simulations by wavefront propagation.

2.3. Energy Storage Application

A new class of miniaturized electrochemical capacitor with high energy densities and high rates capabilities has to be developed for powering the next generation of Internet of things devices. To reach this goal, is proposed to move from a symmetric configuration to a hybrid topology combining a faradic electrode with a capacitive one.^[34,35] Moreover, an attractive solution for miniaturized devices with reduced footprint area consists in depositing thin film electrodes on a high specific surface 3D template.^[12,36] To maximize the amount of active material in 3D miniaturized energy storage devices, the thin film electrodes have to be conformally deposited on 3D scaffold. For that purpose, ALD and sputtering deposition methods were compared to demonstrate the superior capability of the ALD to reach this goal (Table S3, Supporting Information). Recently, nanostructured materials achieving fast lithium ion intercalation via non-diffusion-controlled reaction kinetics were prepared, such as MoO_3 , TiO_2 , or $\text{T-Nb}_2\text{O}_5$.^[37-39] More specifically, it was demonstrated that $\text{T-Nb}_2\text{O}_5$ thin films deposited on a planar substrate by magnetron sputtering and ALD methods exhibit fast intercalation process.^[40,41] However, to the best of our knowledge, the fabrication of 3D $\text{T-Nb}_2\text{O}_5$ electrodes for hybrid miniaturized electrochemical energy storage devices was not demonstrated. Additionally, the nano-CT imaging of nanometer thick $\text{T-Nb}_2\text{O}_5$ films was never reported. For this purpose, films morphology was studied based on a nano-CT analysis of stacked thin films deposited on 3D silicon microtubes scaffold. Morphological and electrochemical characterizations are depicted in **Figure 4** and Figure S4, Supporting Information. We analyse two 3D samples in order to compare the deposition of $\text{T-Nb}_2\text{O}_5$ films by DC magnetron sputtering or ALD on 3D $\text{Si}/\text{Al}_2\text{O}_3/\text{Pt}$ microtubes scaffold. After completion of the electrodes, two $\text{Si}/\text{Al}_2\text{O}_3/\text{Pt}/\text{T-Nb}_2\text{O}_5$ microtubes were extracted from the silicon wafer with a FIB tool and attached to a pin for nano-CT measurements. Two datasets (one per sample) had been collected in fly scan mode at 9.1 keV. Because a spatial resolution of the order of 20 nm is suitable to characterize these engineered materials, 2×2 binning of the CCD pixels was applied. It led to 13.2 nm large isotropic voxels. The volume of the voxels is 16 times bigger than the ones of the FZP datasets described above. This implies an equivalent signal to noise ratio (SNR) that can be maintained with considerably less dose. As a result, the two datasets were

acquired in only 10 and 20 min (“3D acquisitions and reconstructions” section in Supporting Information). The dataset corresponding to the two samples were respectively reconstructed with TomoPy^[42] and the iterative approach used for the FZP datasets.^[33] The SEM cross-section analysis is reported in Figure 4a. From an array of 3D Si microtubes (panel I in Figure 4a), FIB technique is used to isolate and mount a single microtube on a copper grid (panels II and III in Figure 4a). The panel IV of the Figure 4a reveals the sputtered $\text{T-Nb}_2\text{O}_5$ film on $\text{Si}/\text{Al}_2\text{O}_3/\text{Pt}$ current collector. Volume renderings are shown in Figure 4b,c. From Figure 4b, we observe the conformal deposition of the layer of $\text{T-Nb}_2\text{O}_5$ (blue color) deposited by ALD: in that case, the niobium pentoxide film fully coats the platinum layer (red color). In contrast, sputtered $\text{T-Nb}_2\text{O}_5$ film on 3D Si microtube exhibits a non-conformal coating covering only the first micrometer at the top of the tubes (Figure 4c). Figure 4d,e corresponds to portions of selected reconstructed slices underscoring the level of details observable with 13 nm large voxels. One voxel large layer thickness variations and pores smaller than 30 nm are clearly visible. Localized detachments of $\text{T-Nb}_2\text{O}_5$ occurring during the heating process can also be spotted. In order to apply statistics on individual deposited layers, the reconstructed volumes were then segmented into three groups with the Trainable Weka Segmentation plugin,^[43] based on the random forest classification algorithm. Each voxel is attributed either to Pt, $\text{T-Nb}_2\text{O}_5$ or to a larger group encompassing the air, the silicon, and Al_2O_3 . From there, the average thickness of each layer was calculated slice by slice using the exact euclidean distance transform function from the SciPy package.^[44] Depth profiles of the layer average thickness from the top of the tubes are shown in Figure 4f,g. The average layer variation all along the imaged microtube remains smaller than one voxel size (13 nm) approximately close to 40 and 58 nm for the Pt and $\text{T-Nb}_2\text{O}_5$ layers respectively made by ALD. In contrast, the thickness of the sputtered $\text{T-Nb}_2\text{O}_5$ film deposited on the 3D microtube quickly decreases from the top to the bottom of the tube due to the line-of-sight behavior of the MS process: the film completely disappears after $\approx 1.4 \mu\text{m}$. The effect of the microscope point spread function on Pt, that is a high X-ray absorber, tends to blur the contact with the poorly absorbing $\text{T-Nb}_2\text{O}_5$ layer. This makes the separation of these two layers challenging for the segmentation algorithm. It also explains why the average thickness of the $\text{T-Nb}_2\text{O}_5$ sputtered layer plateaus to two voxels even though the total amount of voxel keeps decreasing with depth. To account for segmentation uncertainties, one considers the maximum deposition depth of $\text{T-Nb}_2\text{O}_5$ is 1.4 μm , depth for which the amount of $\text{T-Nb}_2\text{O}_5$ voxels per slice falls below 5% of Pt voxels. These 3D imaging analyses by fast nano-CT technique with nanometer-scale resolution confirm the conformal deposition of $\text{T-Nb}_2\text{O}_5$ by ALD while MS produces a non-conformal layer on 3D silicon scaffold. Electrochemical analysis of 58 nm thick $\text{T-Nb}_2\text{O}_5$ is shown in Figure S4a–c, Supporting Information. Figure S4a, Supporting Information, shows the cyclic voltammetry profile of the film at 1 mV s^{-1} corresponding to the $\text{T-Nb}_2\text{O}_5$ material.^[37] The Nyquist plot at 1.6 V versus Li^+/Li is depicted in Figure S4b, Supporting Information. A vertical line is shown at low frequency while a semicircle is observed at high frequency revealing the charge transfer process. Finally, the evolution of the areal capacity

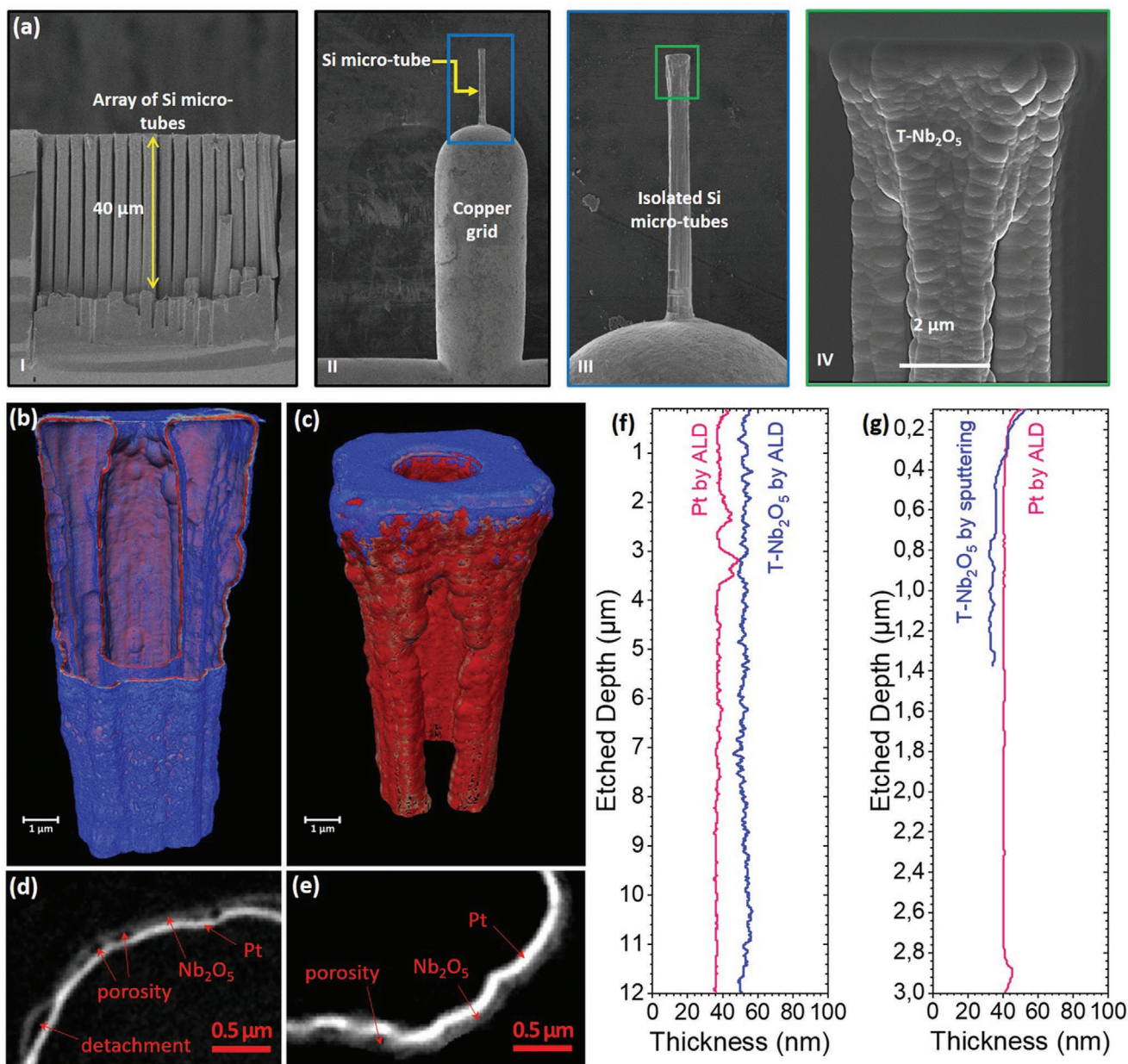


Figure 4. 3D analysis of a 3D electrode. a) FIB preparation and scanning electron microscopy analysis of a 3D electrode. b,c) Volume rendering of T-Nb₂O₅ electrode deposited by ALD (b) and DC magnetron sputtering (c) on Al₂O₃/Pt coated silicon wafer. Pt and T-Nb₂O₅ are respectively represented in blue and red. d,e) Below are zooms on CT slices for the samples engineered with ALD (d) and sputtering (e). f,g) Profiles of the average thickness of Pt and T-Nb₂O₅ in function of the depth from the top of the silicon pillars.

versus the number of cycles is reported in Figure S4c, Supporting Information at different C-rates validating the fast charging process of the T-Nb₂O₅ films.

3. Conclusion

We have demonstrated that the TXM of Sector 32-ID at APS can achieve 10 nm spatial resolution in 3D through FSC estimates as well as direct observations made inside the reconstructed 3D volumes. We also established that nano-CT with transmission

X-ray microscopy is a fast and powerful non-invasive imaging technique for studying the most advanced engineered nano-structured materials and performing failure analysis. Multi-scale characterization of FZP nanolithography objects has been successfully performed, resolving structures and defects whose size is spanning from several micrometers down to 10 nm. High-resolution nano-CT has then been applied to energy materials that are used as high performance electrode in 3D miniaturized electrochemical energy storage devices based on 3D T-Nb₂O₅ films. Our results confirmed the conformal deposition of niobium pentoxide films made by ALD as compared

with that deposited by magnetron sputtering method. Transmission X-ray microscopy has a bright future since there is still a lot of room for improving some of its key components. For instance, promising routes are being explored to fabricate more efficient X-ray objective lenses or direct photon detection cameras with enhanced spatial resolution for full-field imaging. The TXM of 32-ID will also tremendously benefit from the upgrade of the APS to a diffraction-limited storage ring. The new ultralow emittance of the electron-beam combined with the current increase will speed up nano-CT acquisitions by at least one order of magnitude.

4. Experimental Section

Experimental Setup: The 32-ID TXM enabling 10 nm 3D spatial resolution is illustrated in Figure S1, Supporting Information. The transmission X-ray microscopy principle is similar to a visible light microscope (Figure S1a, Supporting Information). Conic illumination of the sample was produced by a condenser. FZPs were used as objective lenses after the sample to magnify radiographies in the X-ray regime. The rotary stage was necessary to perform computed tomography, allowing to acquire sample projections at different angles over 180° scans. Focusing of the condenser and zone plate was made with translations along the optical axis. The TXM at 32-ID was a highly modular instrument. It could accommodate a large range of sample environment cells as well as different kinds of X-ray optics. For instance, the condenser module (Figure S1d, Supporting Information) had 5-axis of motion, 1 m long travel range along the optical axis to accommodate long working distance condensers distances and could overhang above the rotary stage for short working distance large numerical apertures (NA) optics. An adaptor enabled quick condenser optics swapping. The illumination size at the sample location could be controlled with a 3-axis piezo stage moving the condenser in the transverse plane following a defined Lissajou trajectory at high frequency. Those features enabled the use of either grating^[45] or mono-capillary condensers. FZPs were used as objective lenses (Figure S1e, Supporting Information). They were carried on a 200 mm long stroke stick and slip piezo stage enabling positioning of lenses with low to very high NA. In this contribution, 16 nm Δr_N FZP objective lenses made in-house were coupled with a mono-capillary condenser from Sigray Inc. This condenser, with a NA of 5.21 slightly larger than the 4.84 NA of a 16 nm Δr_N FZP objective lenses made in-house are coupled with a mono-capillary condenser. This condenser, with a NA of 5.21 slightly larger than the 4.84 NA of a 16 nm Δr_N FZP at 8 keV, ensured a full illumination of the objective lens. To achieve 10 nm spatial resolution in 3D, a stiff sample stack had been built in-house. The vertical sample positioning and the axis of rotation alignment with respect to the beam were ensured by a robust 2-axis granite air bearing stage (Figure S1c, Supporting Information). Once positions were achieved, air was turned off and the stage behaved like a stiff monolithic block. Objective lens module was attached to a granite pyramid overhanging the rotary stage (Figure S1c,e, Supporting Information). If no drift occurred, the stiff and high precision air bearing rotary stage from Professional Instrument Company (Figure S1c, Supporting Information) enabled tomographic reconstructions without the challenging and slow extra step of projections realignment with software. The microscope was also surrounded by a sound insulated enclosure itself placed in a large experimental hutch with a closed loop system assuring a temperature stability of ± 0.1 °C (Figure S1b, Supporting Information). Information about the size of radiographies after X-ray magnification as well as the depth of focus of the FZP objective lens for different X-ray energies is shown in Table S1, Supporting Information. The DOF of the FZP at 8 keV was 6.6 μm . With a distance sample to detector of 3.5 m, the FOV of radiographies was $11 \times 13 \mu\text{m}^2$. It was possible to perform nano-CT on samples larger than the detector FOV using a stitching approach.^[46] However, the microscope DOF would limit how large a sample could be imaged without observing out of focus artifacts. 3D reconstructions of

an object up to twice as large as a microscope DOF would see limited effects on the final image quality. Imaging thicker specimens would require the use of beyond the depth of focus algorithms.^[47]

3D Data Acquisition: Four tomography datasets were presented in this contribution. They were acquired with a monochromatic beam generated with a Si(111) cryo-cooled double crystals monochromator. The detector assembly comprised a LuAG:Ce scintillator, a 5 \times long working distance Mitutoyo objective lens, and a FLIR CCD (model GS3-U3-51S5M-C). The CCD chip was made of 2448×2048 pixels² with 3.45 μm pixel size. For the FZP and battery datasets, the detector was respectively located 3.5 and 3.4 m downstream the sample, for energies of 8 and 9.1 keV. The obtained magnifications were 224 and 191 leading to an effective pixel size of 5.2 nm for the FZPs and 6.6 nm for the battery datasets. The two datasets from the nanolithography application corresponded to local tomographies of two different 1 μm thick MACE 16 nm Δr_N FZPs. Because the MACE FZPs were fabricated on large silicon windows via etching of the silicon substrate, X-ray transmission through the sample was possible only over a limited angular range of $\pm 70^\circ$. This meant that those datasets had a missing wedge of 40° . The FZP dataset of Figure 2 comprises 5000 projections of 3 s exposure time and has been acquired in 250 min. FSC had been applied on two halves of the dataset, meaning that 10 nm estimates with FSC were achieved on 2500 projections large dataset acquired in 125 min. The second FZP dataset depicted in Figure 3 comprises 2500 projections of 2 s exposure and has been acquired in 85 min. In both cases, high dose was applied to obtain sufficient SNR per voxel whose 5.2 nm width was about twice smaller than the optical resolution of the instrument. It sets the highest spatial resolution achievable to 10.4 nm for the FZPs 3D reconstructions. The two other 3D volumes corresponded to two silicon microtubes from 3D miniaturized electrochemical energy storage devices based on 3D T-Nb₂O₅ films deposited by sputtering and by ALD techniques. Both datasets contained 1210 projections taken with 1 s (ALD, Figure 4a,c) and 0.5 s (sputtering, Figure 4b,d) exposure time and were therefore acquired in 20 and 10 min.

3D Data Reconstruction: Because it is very challenging to keep instrumental nanodrifts below the 10 nm threshold during 1 h long CT-scans, a non-standard method for tomographic reconstructions preventing to degrade the spatial resolution in the 3D volumes was employed. The conventional method for reconstruction was based on using the filtered back-projection (FBP) formula implemented in many software packages including TomoPy,^[42] and Astra Tomography Toolbox.^[48] With this method the object x was recovered from data d by using the following equation

$$x = \mathcal{R}^* \mathcal{W} d \quad (1)$$

where \mathcal{R}^* is the back-projection operator, which is the adjoint to the projection operator \mathcal{R} modeling tomographic data, and \mathcal{W} is a sharpening high-pass filter such as the Ramp or Shepp–Logan filters. The FBP method has the property of amplifying noise in images due to the filter structure. Therefore, reconstruction in many cases is performed by solving the following optimization problem,

$$\min_x \| \mathcal{R}x - d \|_2^2 \quad (2)$$

with using iterative schemes and without any high-pass filtering. Most commonly used methods for solving problem Equation (2) are the conjugate gradients, simultaneous algebraic reconstruction technique, or maximum likelihood expectation maximization.^[49] In order to compensate sample nanodrifts, the technique from ref. [33] was followed and modified the optimization problem Equation (2) with introducing the motion emulation operator D_s that mapped functions to new coordinates according to 2D shifts s . The constrained optimization problem in this case is written as

$$\begin{aligned} \min_{x,s,\psi} & \| D_s \psi - d \|_2^2 \\ \text{subject to} & \mathcal{R}x = \psi \end{aligned} \quad (3)$$

where ψ is an auxiliary variable defining the constraint. Correct estimation of variable s in Equation (3) led to compensating sample drifts and/or deformation for each projection, that in turn resulted in better quality and higher resolution levels of the object reconstruction. According to ref. [33], the optimization problem Equation (3) was solved by using the alternating direction method of multipliers.^[50] with splitting the whole problem into iteratively coordinated local sub-problems with respect to x , s , and ψ . The problems with respect to x and ψ were treated as general L_2 -minimization problems and solved with using the conjugate gradients method, whereas the problem with respect to shifts/deformations s was solved by the optical flow estimation method.^[51] Optical flow is defined as the pattern of apparent motion of image objects between two consecutive frames caused by the object movement, and is commonly used in computer vision for motion tracking algorithms. In Equation (3), the optical flow is found for each projection between the measured data d and the sample re-projections ψ . The whole minimization procedure with coordinated variables x , s , and ψ is iteratively repeated until convergence. The final sample reconstruction demonstrated significantly higher resolution levels (by more than 25%) compared to the results by the standard methods (1) and (2).

Spatial Resolution Estimate: The effective resolution of the X-ray images were estimated by using the Fourier ring correlation (FRC) and Fourier shell correlation (FSC) methods in 2D and 3D cases, respectively.^[32,52,53] The FRC/FSC methods were applied on a pair of independent X-ray measurements or sample reconstructions. As a pair of independent measurements two consecutive radiographs acquired with the same X-ray exposure time were considered. Two independent reconstructions, in turn, were obtained by recovering objects from two independent projection data sets. Then the guiding principle to determine the resolution was to estimate a threshold below which the two objects were inconsistent with one another.^[54] We resort to the 1/2-bit threshold criterion that is imposing as a standard^[32] and has been used to estimate the effective resolution for nanoscale-based imaging techniques.^[55,56] For two objects (2D radiographs or 3D reconstructions) x_1 and x_2 the FRC/FSC curve and the 1/2-bit threshold ($T_{1/2\text{-bit}}$) curve were defined as follows,

$$\text{FRC/FSC}_{x_1, x_2}(r) = \frac{\sum_{r_i \in r} \mathcal{F}x_1(r_i) \overline{\mathcal{F}x_2(r_i)}}{\sqrt{\sum_{r_i \in r} |\mathcal{F}x_1(r_i)|^2 \sum_{r_i \in r} |\mathcal{F}x_2(r_i)|^2}} \quad (4)$$

$$T_{1/2\text{-bit}}(r) = \frac{0.2071 + 1.9102 / \sqrt{n(r)}}{1.2071 + 0.9102 / \sqrt{n(r)}}$$

where summation $\sum_{r_i \in r}$ is performed over all pixels r_i contained in the ring/shell r , and $n(r)$ denotes the number of these pixels. The frequency ring/shell r' for which $\text{FRC/FSC}_{x_1, x_2}(r') = T_{1/2\text{-bit}}(r')$ then gives a half-period spatial resolution $\delta_{1/2\text{-bit}} = 1/2r'$. To find only one intersection with the thresholding curve, the FRC/FSC curve was typically smoothed using locally weighted regression.^[57] For radiographs acquired 20 μm away from the rim of a 16 nm Δr_N FZP depicted in Figure 1d the FRC method results in an effective resolution of 9.4 nm, see Figure 1g. The FRC curve was calculated for the extracted region of the size 1024 \times 1024. Resolution estimation for 3D FZP reconstructions was performed with FSC on a 3D sub-volume also located 20 μm away from a FZP edge as well as with direct observations on 2D reconstructed slices from the outermost zone of a defective FZP. Because of the strong sample anisotropy, a local resolution map covering the entire sample was computed by applying FSC on 20 \times 33 cubic matrices of the size 256³ sliding along an XY grid with 64 voxels steps (Figure 2e). The majority of FSC applied on the 256³ voxels large sub-volumes returns values below 10 nm that were compatible with the direct observations of 10 nm spacing between Pt walls as depicted in Figure 3c–d'.

While using numerical methods like FRC or FSC to estimate the spatial resolution of an image or a 3D volume, it is important to keep in mind the Nyquist theorem which states that a signal should be periodically sampled at a rate at least equal to two times the highest

frequency that needs to be recorded. With images, the sampling rate corresponded to the pixel size, and the smallest resolvable object cannot be smaller than two pixels. Now, it is possible for FRC or FSC to return spatial resolutions better than two pixels/voxels. This implied that images or volumes on which these methods were applied were undersampled. Some studies claim spatial resolution equivalent or close to the voxel size based on FSC results (see Table S2, Supporting Information). But in such cases, the resolution estimate should be leveled up to the size of two voxels. The effects of image undersampling on resolution were addressed and illustrated in Figure S1, Supporting Information, of a soft X-ray ptychography study.^[58] In this contribution, it was shown that well calibrated 28 nm large spherical Fe₃O₄ nanoparticles could not be resolved anymore once the pixel size becomes larger than the sphere radius. Similar demonstration was made with Figures S2 and S3, Supporting Information. Figure S2, Supporting Information, illustrates the well known aliasing effect when objects in an image are smaller than the Nyquist frequency. Figure S3, Supporting Information, underscores how the spatial resolution of one of the FZP datasets would be affected if its voxels size would be twice larger and therefore equivalent to the resolving power of the instrument. Figure S3a, Supporting Information, (copy of Figure 3d) with 5.2 nm large voxels was used to generate Figure S3b, Supporting Information, with a 2 \times 2 binning operation. Figure S3b, Supporting Information, with 10.4 nm voxel size does not resolve correctly the 16 nm large walls that are thinner than two voxels. In addition, objects as close as 10 nm, value equivalent to the resolution estimate with FSC, do not appear anymore separated after binning, as underscored with the two profiles of Figure S3c, Supporting Information.

Comparison of Thin Film Deposition Methods: ALD had the capability to deposit uniform and conformal thin films on complex 3D templates while magnetron sputtering is known as a “line-of-sight” deposition method in microelectronic producing non-conformal films when deposited on complex 3D scaffolds. Table S3, Supporting Information, summarizes the advantages and drawbacks of most of the deposition methods widely used in microelectronic: MS, high power impulse magnetron sputtering (HIPIMS) technology, chemical vapor deposition (CVD), and ALD techniques were compared in terms of growth rate, targeted thickness, conformality, and uniformity. On one hand, PVD techniques such as MS and HIPIMS were known to be fast deposition processes but the conformality of such deposition techniques were not suitable for a perfect coating of functional thin films on 3D complex template. On the other hand, conformality issue was only achieved with CVD deposition method—taking into account a limited aspect ratio (AR = 10:1, see Table S3, Supporting Information)—and with ALD technique considering an interesting AR close to 100:1. The CVD and ALD deposition methods were known to have a low growth rate limiting the thickness of the deposited layers to several hundredth of nanometers for the ALD process.

Preparation of Electrode Samples: First, a dense array of silicon microtubes was fabricated from 3" silicon wafer processed combining photolithography and deep reactive etching technological steps. After the deposition of Al₂O₃ and Pt films by ALD on this 3D scaffold leading to a perfect conformal underlayers coating, this efficient 3D scaffold was covered with thin-film T-Nb₂O₅ electrodes synthesized, either by magnetron sputtering or ALD methods. Niobium pentoxide (T-Nb₂O₅) thin films were deposited by reactive direct current magnetron sputtering (dc-MS) in a CT 200 cluster from Alliance Concept using a metallic niobium target (99.9%, 10 cm diameter, 6 mm thick) under argon and oxygen atmosphere. The distance between the target and the substrate holder was fixed to 60 mm. 110 nm–thick T-Nb₂O₅ film was deposited on a 3D substrate. The deposition was carried out on silicon-based 3D microtubes scaffold ($\phi_{\text{outer}} = 4 \mu\text{m}$, $\phi_{\text{inner}} = 2 \mu\text{m}$, 50 μm depth) coated by layers of Al₂O₃ (thickness = 350 nm) and platinum (thickness = 50 nm). The Al₂O₃ and Pt films were deposited by ALD technique using a Beneq TFS 200 ALD reactor following the procedure of refs. [12,36] T-Nb₂O₅ thin films were grown in a Picosun R200 ALD reactor under an Ar gas pressure around 0.5 mbar. Argon was used as the carrier and purging gas. Niobium(V) ethoxide (Nb(OEt)₅) and deuterated water were used

respectively as niobium precursor and oxygen reactant. Nb(OEt)₅ precursor was purchased from Strem Chemicals (claimed purity 98%). The sublimation temperature was 185 °C for the niobium source while the water source was kept at room temperature. The reactor temperature was fixed at 250 °C. A total of 1000 deposition cycles were achieved to deposit 58 nm-thick amorphous T-Nb₂O₅ thin films (a-Nb₂O₅ layer). The transformation from a-Nb₂O₅ to crystallized, orthorhombic T-Nb₂O₅ polymorph was achieved by thermal annealing at 750 °C during 2 h under air atmosphere of the films. The resulting stacked layers were noted as Si/Al₂O₃/Pt/T-Nb₂O₅.

Methods for Planar and 3D Electrochemical Testing: Electrochemical impedance spectroscopy (EIS) measurements were conducted with a Biologic VMP3 equipment over a frequency range from 10 Hz up to 500 KHz on T-Nb₂O₅ films. Cyclic voltammetry (CV) and galvanostatic charge and discharge plots were investigated on the VMP3 potentiostat/galvanostat equipment using a homemade Teflon like a flat cell with Li metal used as the counter and reference electrode. The electrolyte (1 mL), comprising 1 M LiClO₄ dissolved in ethylene carbonate (EC) and dimethylene carbonate (DMC) in a 1:1 ratio, was poured into the flat-cell cavity. The tested area (circular shape) of the sample was limited to 0.4 cm². The flat cells under test were placed in a glove box with controlled atmosphere (O₂ and H₂O quantities: less than 1 ppm).

Supporting Information

Supporting Information is available from the Wiley Online Library or from the author.

Acknowledgements

This research used resources of the Advanced Photon Source and the Center for Nanoscale Materials, U.S. Department of Energy (DOE) Office of Science User Facilities operated for the DOE Office of Science by Argonne National Laboratory under Contract No. DE-AC02-06CH11357. This research benefited from the financial support of the ANR within the MINOTORES project (ANR-16-CE24-0012-01). The French Renatech network is greatly acknowledged for the microfabrication facilities. The authors also want to thank the French network on electrochemical energy storage (RS2E) and the STORE-EX ANR project for the support.

Conflict of Interest

The authors declare no conflict of interest.

Data Availability Statement

The data that support the findings of this study are available from the corresponding author upon reasonable request.

Keywords

batteries, nanolithography, nanotomography, synchrotrons, transmission X-ray microscopy, X-rays

Received: December 22, 2020

Revised: February 23, 2021

Published online:

- [1] V. De Andrade, A. Deriy, M. J. Wojcik, D. Gürsoy, D. Shu, K. Fezzaa, F. De Carlo, *SPIE News*. **2016**, *10*, 006461.
- [2] J. Andrews, S. Brennan, C. Patty, K. Luening, P. Pianetta, E. Almeida, M. van der Meulen, M. Feser, J. Gelb, J. Rudati, A. Tkachuk, W. Yun W, *Synchrotron Radiat. News* **2008**, *21*, 17.
- [3] I. Greving, F. Wilde, M. Ogurreck, J. Herzen, J. U. Hammel, A. Hipp, F. Friedrich, L. Lottermoser, T. Dose, H. Burmester, M. Müller, F. Beckmann, *Proc. SPIE* **2014**, *9212*, 92120O.
- [4] D. S. Coburn, E. Nazaretski, W. Xu, M. Ge, C. Longo, H. Xu, K. Gofron, Z. Yin, H. H. Chen, Y. Hwu, et al., *Rev. Sci. Instrum.* **2019**, *90*, 053701.
- [5] M. Ogurreck, F. Wilde, J. Herzen, F. Beckmann, V. Nazmov, J. Mohr, A. Haibel, M. Müller, A. Schreyer, *J. Phys.: Conf. Ser.* **2013**, *425*, 182002.
- [6] M. Stampanoni, F. Marone, G. Mikuljan, K. Jefimovs, P. Trtik, J. Vila-Comamala, C. David, R. Abela, *J. Phys.: Conf. Ser.* **2009**, *186*, 012018.
- [7] C. Zhao, T. Wada, V. De Andrade, D. Gürsoy, H. Kato, Y.-c. K. Chen-Wiegart, *Nano Energy* **2018**, *52*, 381.
- [8] S. Müller, P. Pietsch, B.-E. Brandt, P. Baade, V. De Andrade, F. De Carlo, V. Wood, *Nat. Commun.* **2018**, *9*, 2340.
- [9] T. Li, H. Kang, X. Zhou, C. Lim, B. Yan, V. De Andrade, F. De Carlo, L. Zhu, *ACS Appl. Mater. Interfaces* **2018**, *10*, 16927.
- [10] R. Elango, A. Demortière, V. De Andrade, M. Morcrette, V. Seznec, *Adv. Energy Mater.* **2018**, *8*, 1703031.
- [11] E. Eustache, C. Douard, A. Demortière, V. De Andrade, M. Brachet, J. Le Bideau, T. Brousse, C. Lethien, *Adv. Mater. Technol.* **2017**, *2*, 1700126.
- [12] M. Létiche, E. Eustache, J. Freixas, A. Demortière, V. De Andrade, L. Morgenroth, P. Tilmant, F. Vaurette, D. Troadec, P. Roussel, T. Brousse, C. Lethien, *Adv. Energy Mater.* **2017**, *7*, 1601402.
- [13] C. S. Kaira, C. Kantzos, J. J. Williams, V. De Andrade, F. De Carlo, N. Chawla, *Acta Mater.* **2018**, *144*, 419.
- [14] C. S. Kaira, T. J. Stannard, V. De Andrade, F. De Carlo, N. Chawla, *Acta Mater.* **2019**, *176*, 242.
- [15] W. Zhu, F. Fuisseis, H. Lisabeth, T. Xing, X. Xiao, V. De Andrade, S.-i. Karato, *Geophys. Res. Lett.* **2016**, *43*, 9535.
- [16] K. Yuan, V. De Andrade, Z. Feng, N. C. Sturchio, S. S. Lee, P. Fenter, *J. Phys. Chem. C* **2018**, *122*, 2238.
- [17] K. Yuan, V. Starchenko, S. S. Lee, V. De Andrade, D. Gursoy, N. C. Sturchio, P. Fenter, *ACS Earth Space Chem.* **2019**, *3*, 833.
- [18] S. J. Normile, D. C. Sabarirajan, O. Calzada, V. De Andrade, X. Xiao, P. Mandal, D. Y. Parkinson, A. Serov, P. Atanassov, I. V. Zenyuk, *Mater. Today Energy* **2018**, *9*, 187.
- [19] S. Park, J. Bostwick, V. De Andrade, J. Je, *Soft Matter* **2017**, *13*, 8331.
- [20] R. Mizutani, R. Saiga, A. Takeuchi, K. Uesugi, Y. Terada, Y. Suzuki, V. De Andrade, F. De Carlo, S. Takekoshi, C. Inomoto, N. Nakamura, I. Kushima, S. Iritani, N. Ozaki, S. Ide, K. Ikeda, K. Oshima, M. Itokawa, M. Arai, *Transl. Psychiatry* **2019**, *9*, 85.
- [21] T.-Y. Chen, Y.-T. Chen, C.-L. Wang, I. M. Kempson, W.-K. Lee, Y. S. Chu, Y. Hwu, G. Margaritondo, *Opt. Express* **2011**, *19*, 19919.
- [22] I. Mohacsi, I. Vartiainen, B. Rösner, M. Guizar-Sicairos, V. A. Guzenko, I. McNulty, R. Winarski, M. V. Holt, C. David, *Sci. Rep.* **2017**, *7*, 43624.
- [23] J. Wang, Y.-c. Karen Chen, Q. Yuan, A. Tkachuk, C. Erdonmez, B. Hornberger, M. Feser, *Appl. Phys. Lett.* **2012**, *100*, 143107.
- [24] D. A. Grishina, C. A. Hartevelde, A. Pacureanu, D. Devashish, A. Legendijk, P. Cloetens, W. L. Vos, *ACS Nano* **2019**, *13*, 13932.
- [25] G. E. Moore, *IEEE Solid-State Circuits Soc. News*. **2006**, *11*, 33.
- [26] M. Holler, M. Guizar-Sicairos, E. H. Tsai, R. Dinapoli, E. Müller, O. Bunk, J. Raabe, G. Aeppli, *Nature* **2017**, *543*, 402.
- [27] Y.-S. Yu, M. Farmand, C. Kim, Y. Liu, C. P. Grey, F. C. Strobridge, T. Tylicszczak, R. Celestre, P. Denes, J. Joseph, H. Krishnan, F. R. Maia, A. L. Kilcoyne, S. Marchesini, T. P. C. Leite, T. Warwick, H. Padmore, J. Cabana, D. A. Shapiro, *Nat. Commun.* **2018**, *9*, 921.

- [28] W. Chao, B. D. Harteneck, J. A. Liddle, E. H. Anderson, D. T. Attwood, *Nature* **2005**, 435, 1210.
- [29] K. Jefimovs, J. Vila-Comamala, T. Pilvi, J. Raabe, M. Ritala, C. David, *Phys. Rev. Lett.* **2007**, 99, 264801.
- [30] K. Li, M. J. Wojcik, R. Divan, L. E. Ocola, B. Shi, D. Rosenmann, C. Jacobsen, *J. Vac. Sci. Technol., B: Nanotechnol. Microelectron.: Mater., Process., Meas., Phenom.* **2017**, 35, 06G901.
- [31] K. Li, S. Ali, M. Wojcik, V. De Andrade, X. Huang, H. Yan, Y. S. Chu, E. Nazaretski, A. Pattammattel, C. Jacobsen, *Optica* **2020**, 7, 410.
- [32] M. Van Heel, M. Schatz, *J. Struct. Biol.* **2005**, 151, 250.
- [33] V. Nikitin, V. D. Andrade, A. Slyamov, B. J. Gould, Y. Zhang, V. Sampathkumar, N. Kasthuri, D. Gürsoy, F. D. Carlo, *IEEE Transact. Comput. Imaging* **2021**, 7, 272.
- [34] P. Jezowski, O. Crosnier, E. Deunf, P. Poizot, F. Béguin, T. Brousse, *Nat. Mater.* **2018**, 17, 167.
- [35] Y. Shao, M. F. El-Kady, J. Sun, Y. Li, Q. Zhang, M. Zhu, H. Wang, B. Dunn, R. B. Kaner, *Chem. Rev.* **2018**, 118, 9233.
- [36] E. Eustache, P. Tilmant, L. Morgenroth, P. Roussel, G. Patriarche, D. Troadec, N. Rolland, T. Brousse, C. Lethien, *Adv. Energy Mater.* **2014**, 4, 1301612.
- [37] V. Augustyn, J. Come, M. A. Lowe, J. W. Kim, P.-L. Taberna, S. H. Tolbert, H. D. Abruña, P. Simon, B. Dunn, *Nat. Mater.* **2013**, 12, 518.
- [38] H. Sun, L. Mei, J. Liang, Z. Zhao, C. Lee, H. Fei, M. Ding, J. Lau, M. Li, C. Wang, X. Xu, G. Hao, B. Papandrea, I. Shakir, B. Dunn, Y. Huang, X. Duan, *Science* **2017**, 356, 599.
- [39] H.-S. Kim, J. B. Cook, H. Lin, J. S. Ko, S. H. Tolbert, V. Ozolins, B. Dunn, *Nat. Mater.* **2017**, 16, 454.
- [40] C. Arico, S. Ouendi, P.-L. Taberna, P. Roussel, P. Simon, C. Lethien, *ACS Nano* **2019**, 13, 5826.
- [41] S. Ouendi, C. Arico, F. Blanchard, J.-L. Codron, X. Wallart, P. L. Taberna, P. Roussel, L. Clavier, P. Simon, C. Lethien, *Energy Storage Mater.* **2019**, 16, 581.
- [42] D. Gürsoy, F. De Carlo, X. Xiao, C. Jacobsen, *J. Synchrotron Radiat.* **2014**, 21, 1188.
- [43] I. Arganda-Carreras, V. Kaynig, C. Rueden, K. W. Eliceiri, J. Schindelin, A. Cardona, H. Sebastian Seung, *Bioinformatics* **2017**, 33, 2424.
- [44] P. Virtanen, R. Gommers, T. E. Oliphant, M. Haberland, T. Reddy, D. Cournapeau, E. Burovski, P. Peterson, W. Weckesser, J. Bright, S. J. van der Walt, M. Brett, J. Wilson, K. Jarrod Millman, N. Mayorov, A. R. J. Nelson, E. Jones, R. Kern, E. Larson, C. Carey, Í Polat, Y. Feng, E. W. Moore, J. VanderPlas, D. Laxalde, J. Perktold, R. Cimrman, I. Henriksen, E. A. Quintero, C. R. Harris, A. M. Archibald, A. H. Ribeiro, F. Pedregosa, P. van Mulbregt, SciPy 1.0 Contributors, *Nat. Methods* **2020**, 17, 261.
- [45] U. Vogt, M. Lindblom, P. Charalambous, B. Kaulich, T. Wilhein, *Opt. Lett.* **2006**, 31, 1465.
- [46] R. Vescovi, M. Du, V. d. Andrade, W. Scullin, D. Gürsoy, C. Jacobsen, *J. Synchrotron Radiat.* **2018**, 25, 1478.
- [47] M. Du, Y. S. Nashed, S. Kandel, D. Gürsoy, C. Jacobsen, *Sci. Adv.* **2020**, 6, eaay3700.
- [48] W. Van Aarle, W. J. Palenstijn, J. De Beenhouwer, T. Altantzis, S. Bals, K. J. Batenburg, J. Sijbers, *Ultramicroscopy* **2015**, 157, 35.
- [49] F. Natterer, *The Mathematics of Computerized Tomography*, SIAM, Philadelphia, PA, USA **2001**.
- [50] S. Boyd, N. Parikh, E. Chu, B. Peleato, J. Eckstein, *Found. Trends Mach. Learn.* **2011**, 3, 1.
- [51] G. Farnebäck, in *Scandinavian Conf. on Image Analysis*, Springer **2003**, pp. 363–370.
- [52] G. Harauz, M. van Heel, *Optik (Stuttgart)* **1986**, 73, 146.
- [53] S. V. Koho, G. Tortarolo, M. Castello, T. Deguchi, A. Diaspro, G. Vicidomini, *bioRxiv* **2019**, 535583.
- [54] H. Y. Liao, J. Frank, *Structure* **2010**, 18, 768.
- [55] M. Holler, M. Guizar-Sicairos, E. H. Tsai, R. Dinapoli, E. Müller, O. Bunk, J. Raabe, G. Aeppli, *Nature* **2017**, 543, 402.
- [56] M. Holler, A. Díaz, M. Guizar-Sicairos, P. Karvinen, E. Färm, E. Härkönen, M. Ritala, A. Menzel, J. Raabe, O. Bunk, *Sci. Rep.* **2014**, 4, 3857.
- [57] W. S. Cleveland, *J. Am. Stat. Assoc.* **1979**, 74, 829.
- [58] D. A. Shapiro, S. Babin, R. S. Celestre, W. Chao, R. P. Conley, P. Denes, B. Enders, P. Enfedaque, S. James, J. M. Joseph, H. Krishnan, S. Marchesini, K. Muriki, K. Nowrouzi, S. R. Oh, H. Padmore, T. Warwick, L. Yang, V. V. Yashchuk, Y.-S. Yu, J. Zhao, *Sci. Adv.* **2020**, 6, eabc4904.